Supplementary Information

1.Supplementary figures S1 to S7

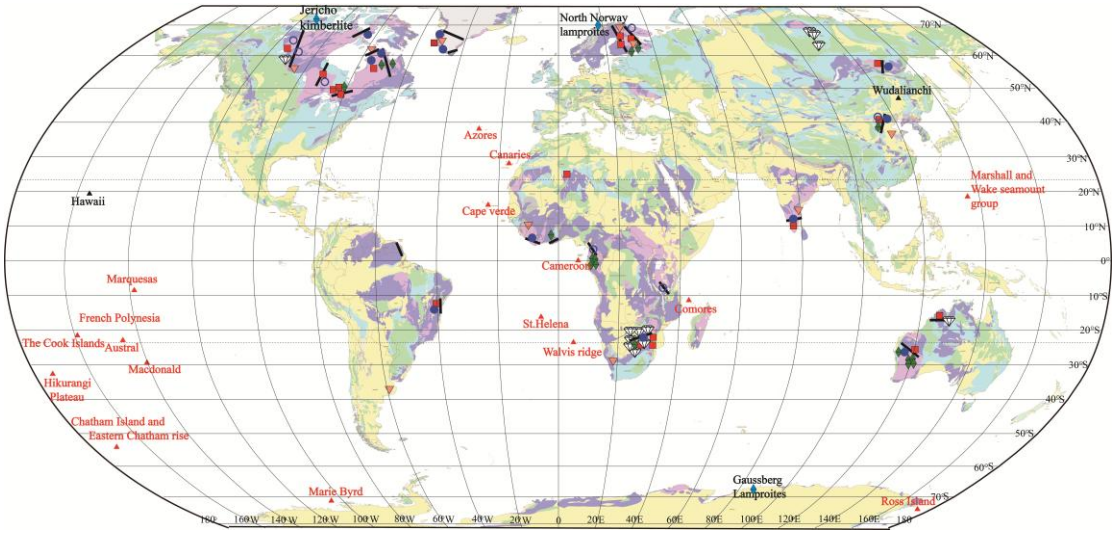

Figure S1: Global Distribution of ocean island basalts, carbonatites, kimberlites, and diamonds This global map showcases the distribution of ocean island basalts, carbonatites, kimberlites, and diamonds included in our study. Adapted from Woolley and Kjarsgaard (2008), it integrates additional information from various sources. The black line outlines the Paleoproterozoic orogenic belt (Zhao et al., 2002). Red triangles indicate HIMU-type basalt (Homrighausen et al., 2018), black triangles represent Cenozoic basalt with a Paleoproterozoic carbonate-bearing source (Huang et al., 2011; Wang et al., 2017; Xu et al., 2020). Diamond icons mark diamond pipes (Howell et al., 2020). Orange inverted triangles denote Paleoproterozoic alkaline basalt, solid blue circles highlight high-pressure Paleoproterozoic granulite (Brown, 2019), hollow blue circles show Paleoproterozoic eclogite locations (Brown, 2019), red squares pinpoint Paleoproterozoic carbonatite sites (Woolley and Kjarsgaard, 2008), green rhombuses represent Paleoproterozoic kimberlite (Tappe et al., 2018), and blue rhombuses indicate Cenozoic kimberlite and lamproite with Paleoproterozoic carbonate-bearing sources (Murphy et al., 2002; Kullerud et al., 2011; Smart et al., 2011).

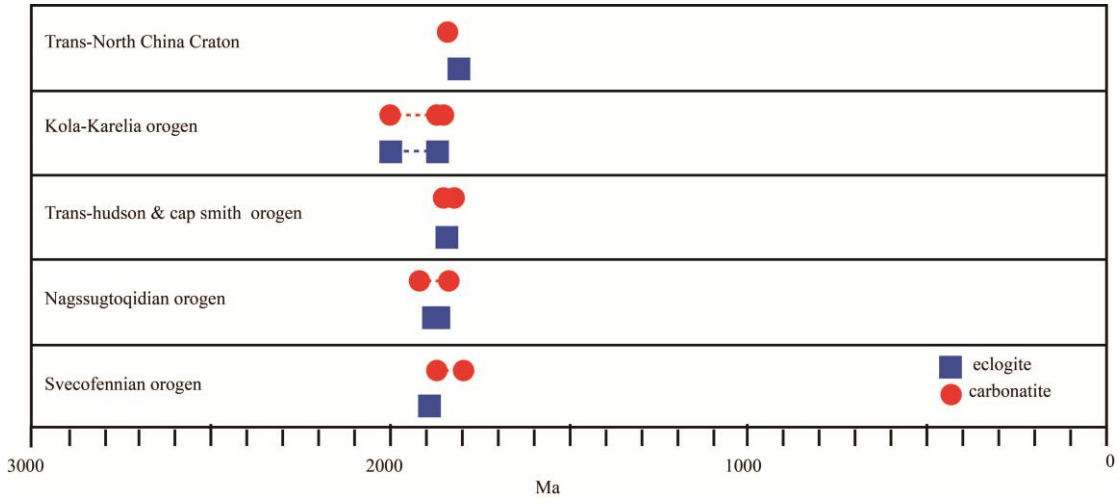

Figure S2: Paleoproterozoic Eclogite and Associated Carbonatite in Orogenic Belts This figure presents the spatial correlation between Paleoproterozoic eclogite (Xu et al., 2018; Li et al., 2023; Weller and St-Onge, 2017; Müller et al., 2018; Smart et al., 2017) and associated carbonatite (see the Supplementary Excel file Sheet 'basalt') within the Paleoproterozoic orogenic belts.

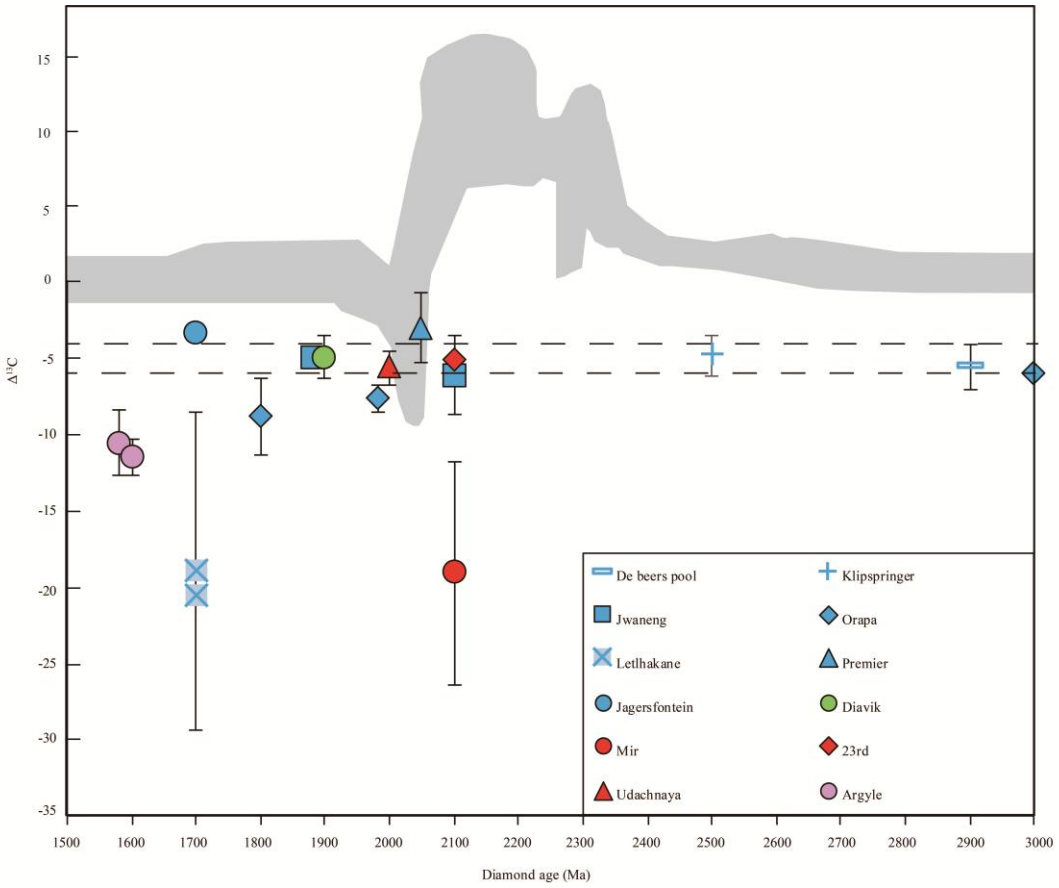

Figure S3: $\delta^{13}C$ Values of Eclogitic Diamond and Carbonate The diagram illustrates the δ13C values of eclogitic diamond (see Supplementary Excel file, Sheet 'diamond') and carbonate. The shadowed area represents the $\delta^{13}C$ values of carbonate (Lyons et al., 2014), while the dashed line delineates the mantle $\delta^{13}C$ range. Blue coloration denotes the Kaapvaal and neighboring Zimbabwe cratons, red for the Siberia craton, pink for the Kimberley craton, and green for the Slave craton.

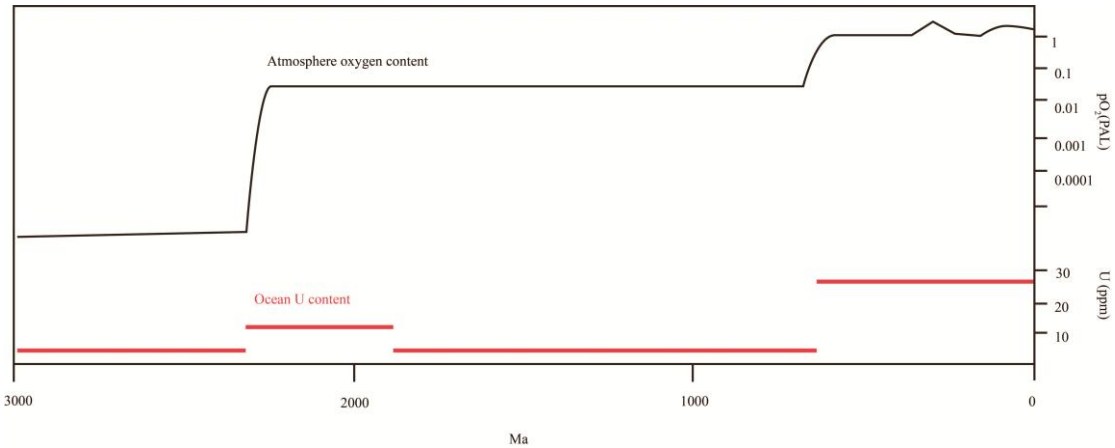

Figure S4: Evolution of Atmospheric Oxygen, and Sediment U Content This figure tracks the evolution of Earth's atmospheric oxygen content, and sediment U contents in black shale records, illustrating evolving ocean redox conditions over time (Lyons et al., 2014).

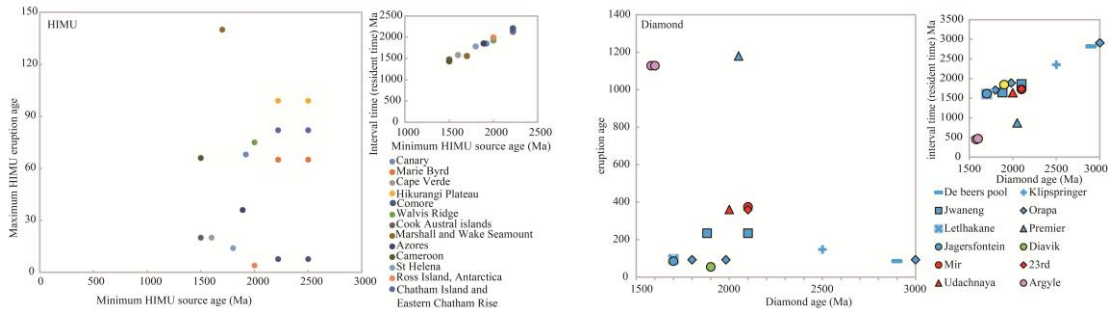

Figure S5: Diamond Age with Kimberlite Eruption Age and HIMU Source Age Range This figure shows the diamond age (see Supplementary Excel file, Sheet 'diamond') juxtaposed with the kimberlite eruption age, along with the minimum and maximum HIMU source ages (see Supplementary Excel file, Sheet 'HIMU'). The carbon residence time of HIMU and diamonds is indicated in the upper right corner. A dashed line represents the minimum age range between 2.22 Ga and 2.5 Ga, marking the disappearance of S-MIF.

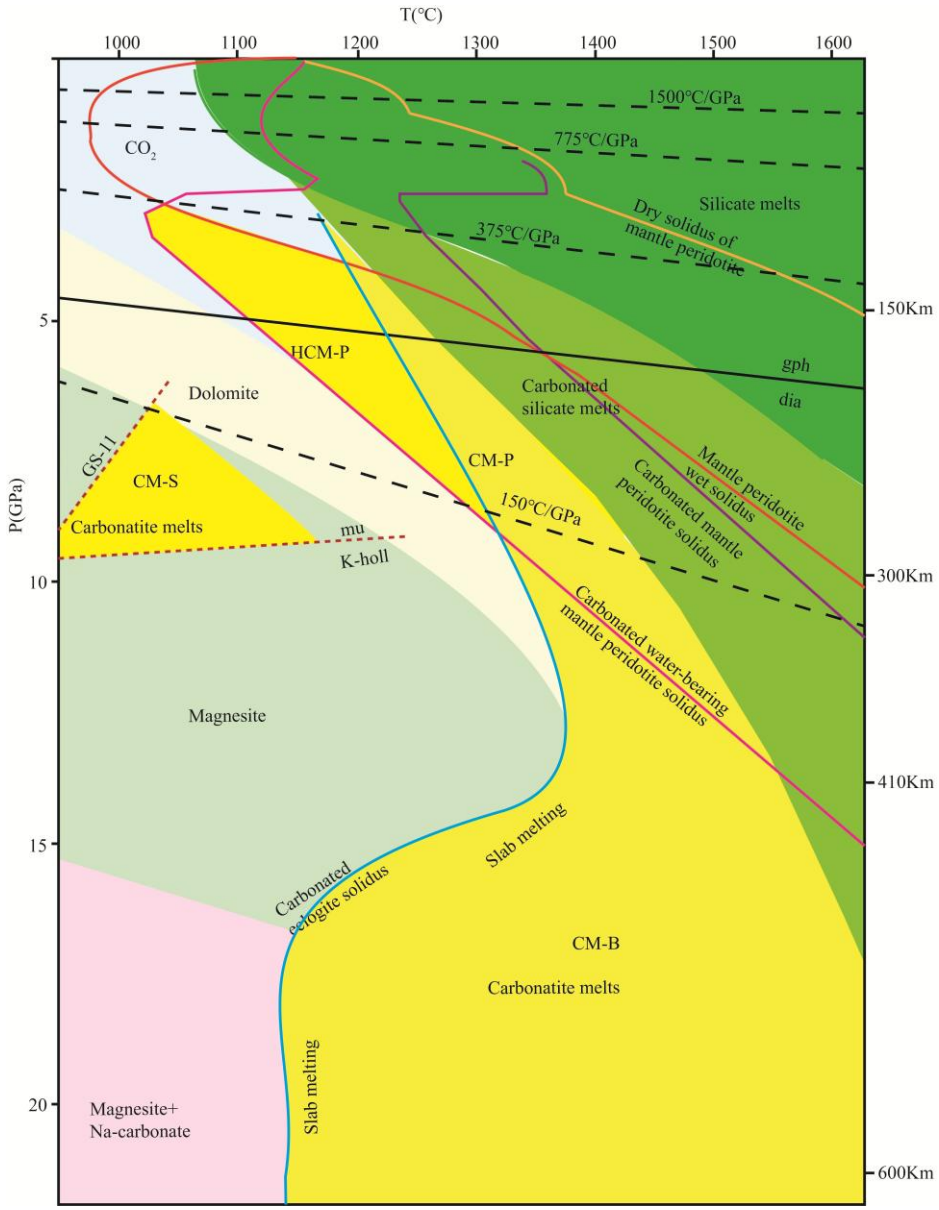

Figure S6: The melting curve of carbonated MORB, carbonated mantle peridotite, and carbonated water-bearing mantle peridotite compared to thermal gradients(Thomson et al., 2016; Brown, 2019; Wei C, 2020). The stability fields of carbon-bearing phases and solidus are identified in different colors. CM-B: carbonatite melts of basalt melting; CM-P: carbonatite melts of peridotite melting HCM-P: hydrous carbonatite melts of peridotite melting; CM-S: carbonatite melts of sediments melting.

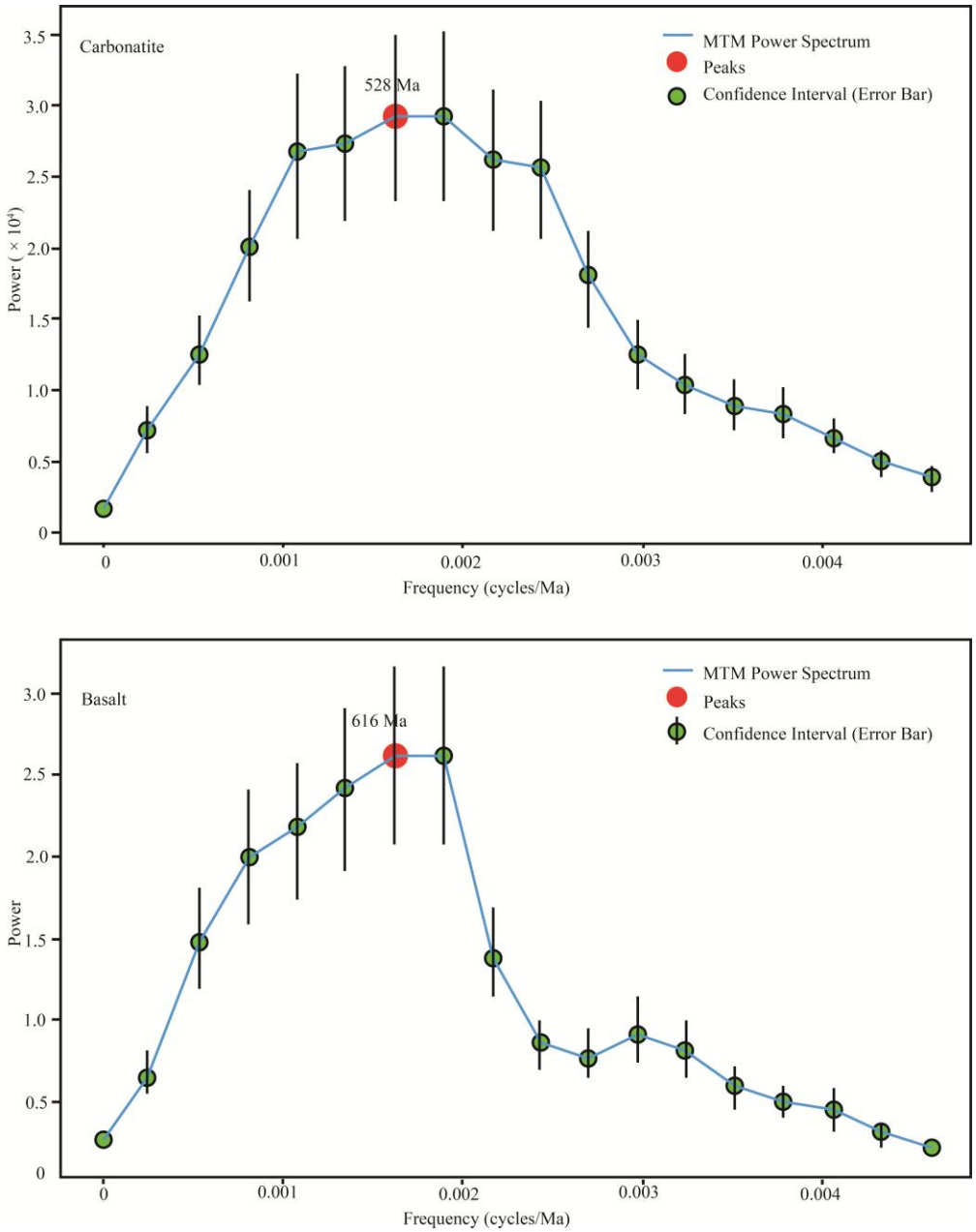

Figure S7: Multi-taper method (MTM) power spectra of carbonatite and basalt curves. The power spectrum calculated using MTM (Multitaper Method) after detrending the average La/Yb values, which were obtained through time-space weighting and Monte Carlo simulation as a function of age in Figure 1. The red points for carbonatite and basalt represent their respective peaks, at 528 Ma and 616 Ma, with power error bars at the 90% confidence interval.

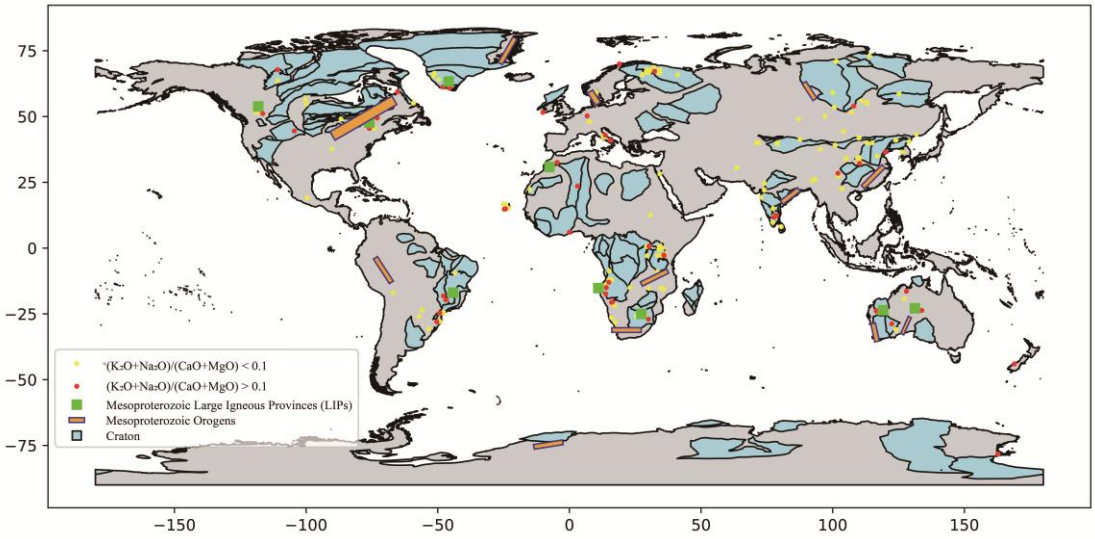

Figure S8: A schematic map of the global distribution of carbonatites with different (K_2O + Na_2O) / (CaO + MgO) ratios. Yellow circles represent carbonatites with a (K_2O + Na_2O) / (CaO + MgO) ratio < 0.1, red circles represent carbonatites with a (K_2O + Na_2O) / (CaO + MgO) ratio > 0.1, green squares represent large igneous provinces from the Mesoproterozoic (Ernst and Youbi, 2017; Zhang et al., 2022), orange rectangles represent orogenic belts from the Mesoproterozoic (Liu et al., 2019), and blue represents cratons (Hasterok et al., 2022).

2. Supplementary tables Basalt to E-type diamond

https://github.com/Lzc02/lithos2025/blob/main/Supplement%20tables.xlsx

References in Supplementary

Woolley, A. R. & Kjarsgaard, B.A. Carbonatite Occurrences of the World: Map and Database. Geological Survey of Canada, Open File 5796 (2008).

Zhao, G., Cawood, P.A., Wilde, S.A. & Sun, M. Review of global 2.1-1.8 Ga orogens: implications for a pre-Rodinia supercontinent. *Earth-Science Reviews* 59, 125–162 (2002).

Homrighausen, S., Hoernle, K., Hauff, F., Geldmacher, J., Wartho, J.A., van den Bogaard, P. & Garbe-Schönberg, D. Global distribution of the HIMU end member: Formation through Archean plume-lid tectonics. *Earth-Science Reviews* (2018). https://doi.org/10.1016/j.earscirev.2018.04.009

Huang, S., Farkaš, J. & Jacobsen, S.B. Stable calcium isotopic compositions of Hawaiian shield lavas: Evidence for recycling of ancient marine carbonates into the mantle. *Geochimica et Cosmochimica Acta* 75, 4987–4997 (2011). https://doi.org/10.1016/j.gca.2011.06.010

Wang, X.J., Chen, L.H., Hofmann, A.W., Mao, F.G., Liu, J.Q., Zhong, Y., Xie, L.W. & Yang, Y.H. Mantle transition zone-derived EM1 component beneath NE China: Geochemical evidence from Cenozoic potassic basalts. *Earth and Planetary Science Letters* 465, 16–28 (2017). https://doi.org/10.1016/j.epsl.2017.02.028

Xu, R., Liu, Y., Wang, X.C., Foley, S.F., Zhang, Y. & Yuan, H. Generation of continental intraplate alkali basalts and implications for deep carbon cycle. *Earth-*

Science Reviews 201, 103073 (2020). https://doi.org/10.1016/j.earscirev.2020.103073
Howell, D., Stachel, T., Stern, R.A., Pearson, D.G., Nestola, F., Hardman, M.F., Harris, J.W., Jaques, A.L., Shirey, S.B., Cartigny, P., Smit, K.V., Aulbach, S., Brenker, F.E., Jacob, D.E., Thomassot, E., Walter, M.J. & Navon, O. Deep carbon through time: Earth's diamond record and its implications for carbon cycling and fluid speciation in the mantle. *Geochimica et Cosmochimica Acta* 275, 99–122 (2020). https://doi.org/10.1016/j.gca.2020.02.011
Brown, M. Secular change in metamorphism and the onset of global plate tectonics. *American Mineralogist* 103, 181–196 (2019).
Tappe, S., Smart, K., Torsvik, T., Massuyeau, M. & de Wit, M. Geodynamics of kimberlites on a cooling Earth: Clues to plate tectonic evolution and deep volatile cycles. *Earth and Planetary Science Letters* 484, 1–14 (2018). https://doi.org/10.1016/j.epsl.2017.12.013
Murphy, D.T., Collerson, K.D. & Kamber, B.S. Lamproites from Gaussberg, Antarctica: Possible transition zone melts of Archaean subducted sediments. *Journal of Petrology* 43, 981–1001 (2002). https://doi.org/10.1093/petrology/43.6.981
Kullerud, K., Zozulya, D., Bergh, S.G., Hansen, H. & Ravna, E.J.K. Geochemistry and tectonic setting of a lamproite dyke in Kvaløya, North Norway. *Lithos* 126, 278–289 (2011). https://doi.org/10.1016/j.lithos.2011.08.002
Smart, K.A., Chacko, T., Stachel, T., Muehlenbachs, K. & Stern, R.A. Diamond growth from oxidized carbon sources beneath the Northern Slave Craton, Canada: A δ13C-N study of eclogite-hosted diamonds from the Jericho kimberlite. *Geochimica et Cosmochimica Acta* 75, 6027–6047 (2011). https://doi.org/10.1016/j.gca.2011.07.028
Li, X., Zhang, L., Wei, C., Bader, T. & Guo, J. Cold subduction recorded by the 1.9 Ga Salma eclogite in Belomorian Province (Russia). *Earth and Planetary Science Letters* 602, 117930 (2023). https://doi.org/10.1016/j.epsl.2022.117930
Weller, O.M. & St-Onge, M.R. Record of modern-style plate tectonics in the Palaeoproterozoic Trans-Hudson orogen. *Nature Geoscience* 10, 305–311 (2017). https://doi.org/10.1038/ngeo2904
Müller, S., Dziggel, A., Sindern, S., Kokfelt, T.F., Gerdes, A. & Kolb, J. Age and temperature-time evolution of retrogressed eclogite-facies rocks in the Paleoproterozoic Nagssugtoqidian Orogen, South-East Greenland: Constrained from U-Pb dating of zircon, monazite, titanite and rutile. *Precambrian Research* 314, 468–486 (2018). https://doi.org/10.1016/j.precamres.2018.07.002
Smart, K.A., Cartigny, P., Tappe, S., O'Brien, H. & Klemme, S. Lithospheric diamond formation as a consequence of methane-rich volatile flooding: An example from diamondiferous eclogite xenoliths of the Karelian craton (Finland). *Geochimica et Cosmochimica Acta* 206, 312–342 (2017). https://doi.org/10.1016/j.gca.2017.03.014
Lyons, T.W., Reinhard, C.T. & Planavsky, N.J. The rise of oxygen in Earth's early ocean and atmosphere. *Nature* 506, 307–315 (2014). https://doi.org/10.1038/nature13068
Thomson, A.R., Walter, M.J., Kohn, S.C. & Brooker, R.A. Slab melting as a barrier to deep carbon subduction. *Nature* 529, 76–79 (2016). https://doi.org/10.1038/nature16174

Wei, C. & Zheng, Y. Metamorphism, fluid behavior and magmatism in oceanic subduction zones. *Science China Earth Sciences* 63, 52–77 (2020). https://doi.org/10.1007/s11430-019-9482-y

Ernst, R.E., Youbi, N., 2017. How Large Igneous Provinces affect global climate, sometimes cause mass extinctions, and represent natural markers in the geological record. Palaeogeogr. Palaeoclimatol. Palaeoecol. 478, 30–52. https://doi.org/10.1016/j.palaeo.2017.03.014

Hasterok, D., Halpin, J.A., Collins, A.S., Hand, M., Kreemer, C., Gard, M.G., Glorie, S., 2022. New Maps of Global Geological Provinces and Tectonic Plates. Earth-Science Rev. 231. https://doi.org/10.1016/j.earscirev.2022.104069

Liu, C., Runyon, S.E., Knoll, A.H., Hazen, R.M., 2019. The same and not the same: Ore geology, mineralogy and geochemistry of Rodinia assembly versus other supercontinents. Earth-Science Rev. https://doi.org/10.1016/j.earscirev.2019.05.004

Martin, L.H.J., Schmidt, M.W., Mattsson, H.B., Guenther, D., 2013. Element Partitioning between Immiscible Carbonatite and Silicate Melts for Dry and H2O-bearing Systems at 1-3gpa. J. Petrol. 54, 2301–2338. https://doi.org/10.1093/petrology/egt048

Zhang, S.H., Ernst, R.E., Munson, T.J., Pei, J., Hu, G., Liu, J.M., Zhang, Q.Q., Cai, Y.H., Zhao, Y., 2022. Comparisons of the Paleo-Mesoproterozoic large igneous provinces and black shales in the North China and North Australian cratons. Fundam. Res. 2, 84–100. https://doi.org/10.1016/j.fmre.2021.10.009